Chapter 2
Visualization and Numerical Investigation of Natural Convection Flow of CO_2 in Aqueous and Oleic Systems

Abstract Optimal storage of carbon dioxide (CO_2) in aquifers requires dissolution in the aqueous phase. Nevertheless, transfer of CO_2 from the gas phase to the aqueous phase would be slow if it were only driven by diffusion. Dissolution of CO_2 in water forms a mixture that is denser than the original water or brine. This causes a local density increase, which induces natural convection currents accelerating the rate of CO_2 dissolution. The same mechanism also applies to carbon dioxide enhanced oil recovery. This study compares numerical models with a set of high pressure visual experiments, based on the Schlieren technique, in which we observe the effect of gravity-induced fingers when sub- and super-critical CO_2 at in situ pressures and temperatures is brought above the liquid, i.e., water, brine or oil. A short but comprehensive description of the Schlieren set-up and the transparent pressure cell is presented. The Schlieren set-up is capable of visualizing instabilities in natural convection flows; a drawback is that it can only be practically applied in bulk flow, i.e., in the absence of a porous medium. All the same many features that occur in a porous medium also occur in bulk, e.g., unstable gravity fingering. The experiments show that natural convection currents are weakest in highly concentrated brine and strongest in oil, due to the higher and lower density contrasts respectively. Therefore, the set-up can screen aqueous salt solutions or oil for the relative importance of natural convection flows. The Schlieren pattern consists of a dark region near the equator and a lighter region below it. The dark region indicates a region where the refractive index increases downward, either due to the presence of a gas liquid interface, or due to the thin diffusion layer, which also appears in numerical simulations. The experiments demonstrate the initiation and development of the gravity induced fingers. The experimental results are compared to numerical results. It is shown that natural convection effects are stronger in cases of high density differences. However, due to numerical limitations, the simulations are characterized by much larger fingers.

Keywords CO_2 sequestration · Dissolution trapping · Natural convection · Fluid · Visualization · Schlieren technique

Published in: Petroleum Science and Engineering volume 122, October 2014, pages 230–239 and COMSOL 2012.

© Springer International Publishing Switzerland 2016

R. Khosrokhavar, *Mechanisms for CO_2 Sequestration in Geological Formations and Enhanced Gas Recovery*, Springer Theses, DOI 10.1007/978-3-319-23087-0_2

Nomenclature

C	concentration (mol/m^3)
C_g	concentration (mol/m^3)
D	molecular diffusion coefficient, (m^2/ s)
D_g	molecular diffusion coefficient in gas phase, (m^2/ s)
K	permeability, mD
β	volumetric expansion coefficient (m^3/mol)
V	velocity (m/s)
P	pressure (bar)
t	time
v	kinematic viscosity (m^2/s)
ρ	density (kg/m^3)
A	the area exposed to CO_2 (m^2)
μ	viscosity of the solvent (kg.m.s)
g	acceleration due to gravity (kg/m)
Ra	Rayleigh number
K_H	Henry's constant
n	refractive index
n_w	refractive index of pure water
n_{CO_2}	refractive index of pure CO_2
$\rho_w^{(0)}$	density of pure water at the reference temperature(kg/m^3)
α	polarizability
L	Avogadro's number
m_{w,CO_2}	molality of carbon dioxide in the water phase(mol/kg)
γ_{w,CO_2}	activity coefficient
$f_{g,CO_2(g)}$	fugacity of carbon dioxide in the gas phase(bar)

Subscripts

0	reference value of the quantity
g	gas
i	initial value
w	water

2.1 Introduction

The Optimal storage [1] of carbon dioxide (CO_2) in aquifers requires dissolution of CO_2 in formation brine because the virtual density of dissolved CO_2 in water (1333 kg/m^3) is more favorable than its density in the supercritical gas-phase. Without dissolution of CO_2 in the aqueous phase the storage volume of CO_2 in aquifers would be of the order of 2 % of the reservoir volume [2]. It is expected

that, due to buoyancy forces, injected CO_2 rises to the top of the reservoir forming a gas layer. Transfer from the gas layer to the aquifer below would be slow if it were only driven by molecular diffusion. However, CO_2 mixes with the water (or brine) to form a denser aqueous phase (e.g., in pure water $\Delta\rho \sim 8$ kg/m^3 at 30 bar, see, [3]). This initiates convective currents and increases the dissolution rate, and thus dissolution of larger amounts of CO_2 in a shorter period of time.

Underground storage of CO_2 involves costly processes. First, the flue gas should be captured; its CO_2 fraction should be separated, transported to the injection site, and finally compressed and stored in the geological formation. A cost-effective approach may then be to use carbon dioxide enhanced oil recovery, which at the same time also stores part of the injected CO_2. Moreover, one of the challenges in the application of CO_2-based enhanced oil recovery techniques for naturally fractured reservoirs is the slow mass transfer between the carbon dioxide in the fracture and the crude oil in the matrix. As carbon dioxide is miscible with oil and causes a density increase of oil, natural convection phenomena could promote the transfer rates, increase the mixing between the carbon dioxide and the oil, and accelerate the oil production. Therefore, understanding the CO_2-oil interaction during these processes is of great interest for the petroleum industry. The initial stage of natural convection in a saturated porous layer with a denser fluid on top of a lighter fluid has been extensively studied by means of linear stability analysis, numerical simulations and the energy method [4–17]. These analyses provide the criteria under which the boundary layer saturated with CO_2 becomes unstable. The results are usually expressed in terms of the Rayleigh number, which is dependent on the fluid and porous media properties and is defined as

$$Ra = \frac{k\Delta\rho g H}{\varphi \mu D} \tag{2.1}$$

where k [m^2] is the permeability of the porous medium, $\Delta\rho$ [kg/m^3] is the characteristic density difference between the mixture and the fresh water, g [m/s^2] is the acceleration due to gravity, H [m] is the characteristic length of the system, $\varphi[-]$ is the porosity, μ [Pa.s] is the viscosity of the mixture, and D [m^2/s] is the molecular diffusion coefficient of CO_2 in water. It has been shown that the critical time required for the onset of the convective currents is inversely related to the square of Ra, i.e., $t_c \propto Ra^{-2}$ [13, 16]. The critical wavelength of the fastest growing finger scales with the inverse of Rayleigh number, i.e., $\lambda_c \propto Ra^{-1}$. Lapwood [18] showed that the interface will be unstable for Rayleigh numbers above $4\pi^2 \approx 40$ in porous media. In the absence of a porous medium (for bulk solutions), k in Eq. (2.1) is replaced by H^2 and natural convection occurs when $Ra > 2100$. It can be expected that the effect will be more pronounced for bulk solutions; however, for the time scales relevant for geological storage of CO_2 the effect will be also significant in porous media. There are many papers devoted to the theoretical description of convection currents during storage of CO_2 in aquifers; the effect was first mentioned by [19]. Mass transfer of CO_2 into water has been evaluated experimentally and

analytically at different conditions. References [20–23] investigate the occurrence of natural convection by recording the pressure change in a cylindrical PVT-cell, where a fixed volume of CO_2 gas was brought into contact with a column of distilled water. The experimental results show that initially the mass-transfer rate is much faster than predicted by Fick's Law (diffusion-based model) indicating that another mechanism apart from molecular diffusion plays a role. It was conjectured that density-driven natural convection enhances the mass-transfer rate. This conjecture could be validated by comparison of experimental data with a numerical model that couples mass- and momentum conservation equations [22, 24]. Figure 2.1 compares the extent of natural convection in the presence and absence of a porous medium in a glass tube with a radius of 3.5 mm by measuring the pressure history. In one experiment the glass tube is filled with only water, and in the other one the tube is filled with a porous medium of the same height and saturated with water. The figure shows that, although natural convection enhances the transfer rate in water-saturated porous media, its enhancement is less than in a bulk liquid.

Okhotsimskiis et al. [25] visualized the convective currents in a binary CO_2-water system and qualitatively evaluated the experimental results, based on Marangoni and free (or natural) convection effects, in bulk modules of gas and liquid. More recently, Kneafsey and Pruess [26] visualized the occurrence of fingers in the CO_2-water system at low pressures.

The objective of this chapter is to design and construct an experimental set-up, by which the development and growth of fingers of CO_2 in the aqueous and oleic phases at high pressure can be visualized. Because the density gradient plays the main role in occurrence of the convective currents, the Schlieren method has been used to visualize the phenomenon. By applying COMSOL Multiphysics the numeric results are compared with the experiment.

The structure of the chapter is as follows: first we describe our experimental Schlieren set-up and briefly explain the procedure. Then we illustrate the theoretical

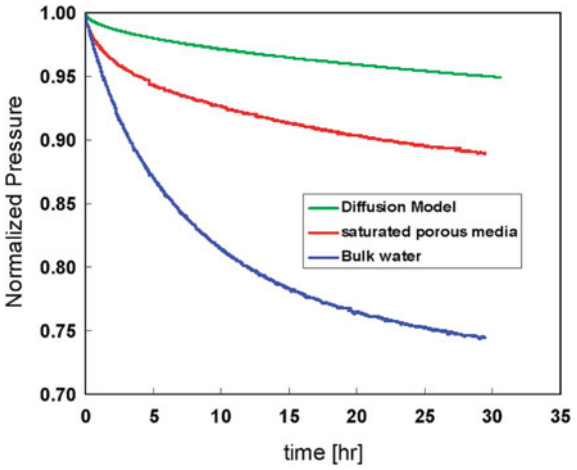


Fig. 2.1 Comparison of the pressure history of the experiments with (*red*) and without porous media (*blue*). The green curve is based on a diffusion model in the absence of convection. The experiments were done in a glass tube with radius of 3.5 mm at 11 bar [21]

model that describes the natural convection flow in our experimental configuration. Later we provide a derivation to connect the refractive index gradient $\partial_z n$ to the concentration gradient $\partial_z c$, which can be used in the interpretation of the experiments. Afterwards, we present our experimental and numerical results. Finally we end the chapter with some concluding remarks.

2.2 Experimental Setup

The main aim of the chapter is to visualize the induced convection currents when carbon dioxide is brought above a layer of liquid water, brine or oil. These currents originate because the density of the CO_2-liquid mixtures is higher than the pure liquid. It results in gravitationally-unstable flows in the CO_2-water (water and brine) or CO_2-oil mixtures. Our method of choice is the Schlieren method, because it is relatively simple to implement, it can be applied at high pressures and under favorable circumstances can be compared to numerical simulation data.

The Schlieren method (for more details see [27]) is an optical technique that can be applied to detect density gradients during fluid flow. The schematic of the Schlieren set-up is shown in Fig. 2.2. To create a point source a 200 W light source is used behind an aperture diaphragm with an opening of 0.5 mm. The parallel light beam is created by locating the point source at a focal point of the first achromatic lens. This lens has a focal length of 1500 mm and a diameter of 110 mm. Because an achromatic lens (optical properties more or less independent of the wavelength of the light) is used, the chromatic aberration effect is minimized. In our Schlieren set-up, the distance between the light source and the Schlieren object, i.e., the high pressure cell (see Figs. 2.2 and 2.3) is about 1.6 m. In the high pressure cell the light rays will be deflected due to the gradients in refractive index caused by the variations in CO_2 concentration. Then the partially deflected light beam converges in the focal plane of the second achromatic lens. This lens is identical to the first achromatic lens. A metal piece with a fine thickness is used as a knife edge on the focal plane of the second lens. The effect of the knife edge can be understood as follows. The light deflected by the inhomogeneity in CO_2 concentration will not be focused in the focal point, but rather will be displaced in the focal plane of the second lens. This means the deflected light rays are shifted with respect to the knife edge, which causes a change in the light transmission by the knife edge and consequently the recorded image intensity. In the present implementation the knife edge is placed horizontally, which results in the system to be sensitive to light deflections in the vertical directions, hence vertical gradients in CO_2 concentration. To record the Schlieren images, one black and white, CCD camera (Lavision-Imager intense) is used. The exposure time for the camera was set to 1 s to record the images with a resolution of 1000×1000 pixels.

Figure 2.3 shows a schematic representation of the high pressure cell that can sustain 150 bar. The cell consists of a stainless steel frame with a cylindrical hole. Inside the hole there is a stainless steel cylinder bounded by two flanges.

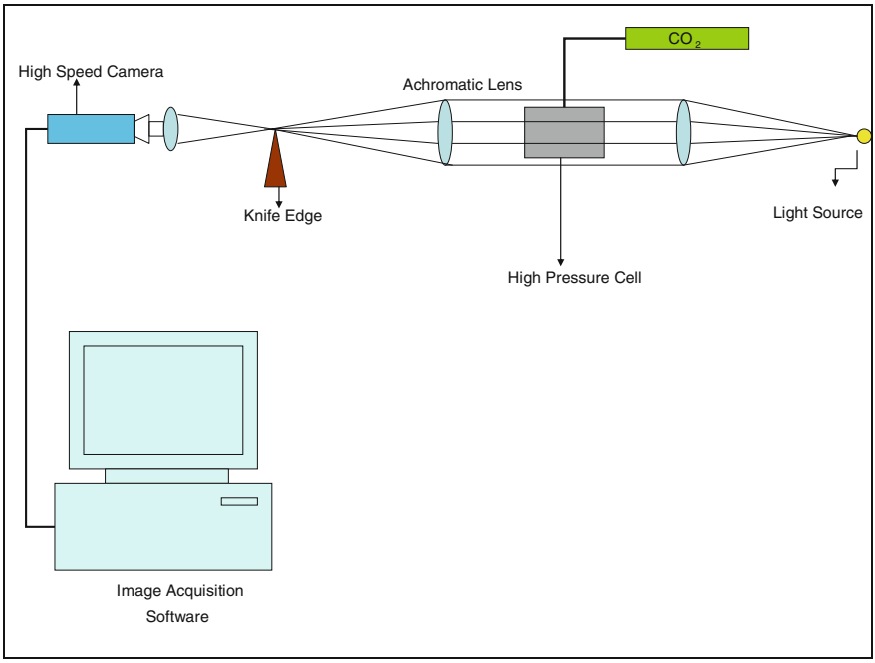


Fig. 2.2 Schematic drawing of Schlieren set up on a vibration suppressing table. A horizontal knife edge is applied from the side. The high speed camera captures the intensity image. The deviation of the intensity is a measure of the concentration gradient in the z-direction perpendicular to the table (see Eq. (2.13))

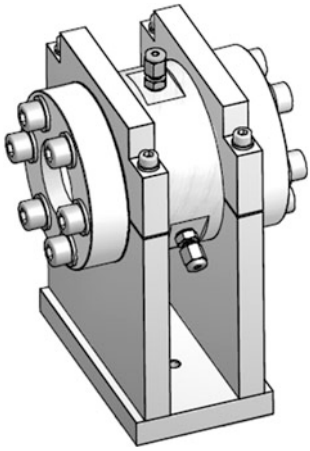


Fig. 2.3 Cylindrical high pressure cell, in a holder, with two windows of thickness 25.4 mm

The cylinder has an outer diameter of 72 mm and a length of 122 mm. The two flanges on each side have the same inner and outer diameter as the cell. The length of the flanges is 22 mm. Between the flanges there are two glass windows with a

diameter of 51 mm and a length of 25.4 mm. Between the two windows there is a gap of 11.6 mm and diameter of 25 mm that can contain the fluids. The gap has four connections, of which two are visible in Fig. 2.3. The other two connections are at the bottom and symmetrically at the other side. The bottom connector is used to bring water inside the high pressure cell; the top connector for filling the cell with CO_2. One side connector is used to record the pressure with a pressure transducer (PTX611, DRUCK, ±0.08 % of span) and simultaneously to insert a thermocouple that measures the temperature in the upper half of the cell. The thermocouple and pressure transducer stick half a centimeter in the cell one centimeter above the equator. Another thermocouple is inserted in the other side connector and also measures the temperature in the upper half of the cell, in the exact mirror position of the other thermocouple. A heating wire was mounted around the cell to keep the cell at a constant temperature of 39 °C.

Before usage, the windows are rinsed to make them as clean as possible. Initially the bottom half of the cell is filled with the aqueous or oleic phase. Subsequently gas is admitted from the top until the required pressures of 64 and 84 bar are reached. The gas in the container used to carry out the experiments consists of 99.98 % pure carbon dioxide. There is one computer for recording the pressure history and one for recording the images with the high speed camera.

2.3 Numerical Modeling

For the modeling we consider a 3-D model for natural convection flow of CO_2 in the aqueous or oleic phase (see Fig. 2.4). The flow cell is a horizontal cylinder, of which the lower half is filled with brine or oil. The diameter of the fluid containing part of the cell is 25 mm and the length is 11.6 mm as in the experiment. The cell is filled with liquid until the equator. The CO_2 gas is brought on top of the liquid, after

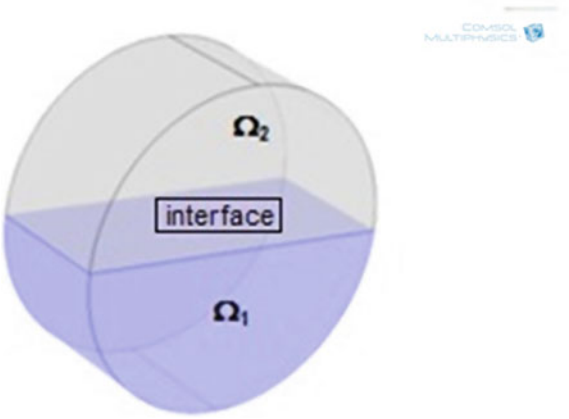


Fig. 2.4 Geometry of the model

which natural convection starts. We applied the conventional equations for buoyant density flow and the Boussinesq approximation. This approximation uses constant densities except in the gravity term in the Navier Stokes equation. Due to the density heterogeneity the fresh (CO_2-free) liquid moves to the interface and CO_2 containing liquid moves downwards, accelerating the mass transfer rate. The boundary conditions are no flow conditions at the vessel boundary.

2.4 Governing Equations

We consider a three-dimensional configuration of the horizontal cylinder (Fig. 2.4). The vertical coordinate is the z-direction, whereas the horizontal coordinate is the x-direction. The coordinate perpendicular to the paper is the y-direction. The thickness of the interface is 11.6 mm in the y-direction. More details are given in this paper in the section where we explain the experimental set up. For the ease of reference, a brief description is written here. There are two parts in our cylindrical model. The upper part (Ω_2) is filled with the gas phase and the lower part (Ω_1) is filled with liquid. The governing equations in both domains of the cell are given below.

Liquid Phase Equations in Ω_1:

(a) Continuity Equation:

$$\text{div } \mathbf{v} = 0 \tag{2.2}$$

(b) Conservation of Momentum, disregarding inertia effects:

$$\frac{\partial \mathbf{v}}{\partial t} = -\frac{1}{\rho}\mathbf{grad}p + v\,\Delta\mathbf{v} - \beta_c g \Delta c \tag{2.3}$$

(c) Concentration Equation:

$$\frac{\partial c}{\partial t} + \mathbf{v}\,.\,\mathbf{grad}\ c = D\Delta c \tag{2.4}$$

Gas Phase Equations in Ω2:

$$\frac{\partial c_g}{\partial t} = D_g \Delta c_g \tag{2.5}$$

Boundary and initial conditions for the liquid phase:

Initially, there is no CO_2 dissolved in the liquid, i.e. for t = 0, and (x, y, z)$\in \Re^3$

$w = v = u = c = 0$

The boundary conditions of the model are: We use zero velocity and zero flux conditions at all boundaries except for the interface between gas and liquid. At this

boundary we use Henry's law to relate the gas pressure to the carbon dioxide concentration in the liquid, i.e.,

$$K_{w-g}^{H} = a_{w,CO_2}/a_{g,CO_2} = m_{w,CO_2}\gamma_{w,CO_2}/f_{g,CO_2}\ , \tag{2.6}$$

where m_{w,CO_2} is the molality of carbon dioxide in the water phase, y_{w,CO_2} the activity coefficient, and $f_{g,CO_2(g)}$ is the fugacity of carbon dioxide in the gas phase. We use PHREEQC [28] for the computations. The procedure to get activities in neutral molecules is given [29].

Boundary and initial conditions for the gas phase:

Initially at $t = 0$,

$$C_g = \frac{f_{g,CO_2}}{R_B T}, \tag{2.7}$$

Figures 2.5 and 2.6 present results obtained by PHREEQC [28] for pure water, n-decane, brine with 25 w/w% salt and 10 w/w%.

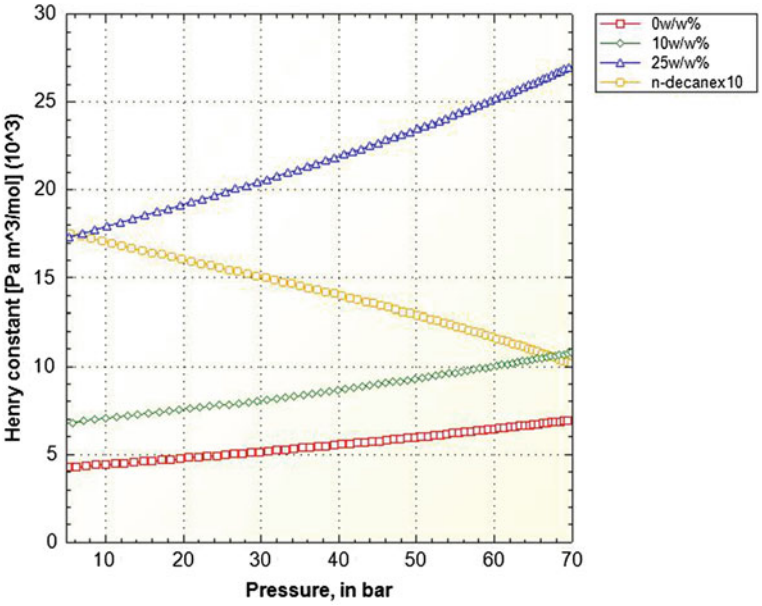


Fig. 2.5 Henry's constant for a 25 w/w% and a 10 w/w% NaCl solution, fresh water and oil versus pressure. For n-Decane, the displayed Henry constant should be divided by 10

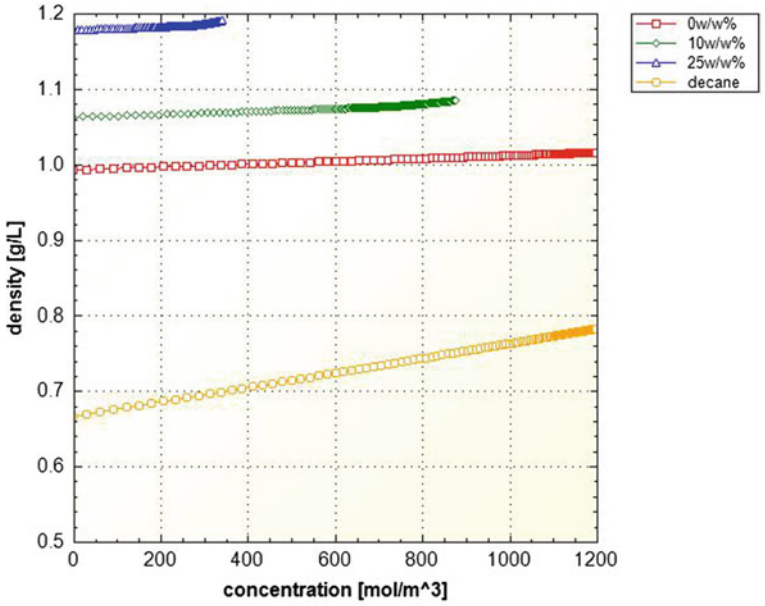


Fig. 2.6 The density [g/L] of a 25 w/w%, a 10 w/w% NaCl solution, fresh water and oil versus dissolved C(4) concentration at T = 312 k. By C (4) we mean the sum of the CO_2, CO_3^{2-}, HCO_3^- at elevated level). For n-Decane the dissolved concentration on the horizontal axis should be multiplied to 10

2.5 Theory

Here, we follow [30, 31] to obtain a relation between the refractive index gradient and concentration gradient. By way of example we give here the derivation for pure water. We start with an equation that relates the refractive index of the solution to the refractive indexes of the components, i.e.,

$$\frac{n^2-1}{n^2+2} = \upsilon_w \frac{n_w^2-1}{n_w^2+2} + (1-\upsilon_w)\frac{n_{CO_2}^2-1}{n_{CO_2}^2+2}, \tag{2.8}$$

where n is the refractive index of the mixture, n_w is the refractive index of pure water, and n_{CO_2} is the refractive index of "pure CO_2" if it were existing as a single pure component. We use $\upsilon_w = \rho_w/\rho_w^{(0)}$ to denote the volume fraction of water in the mixture. Therefore, Eq. (2.8) can be converted to:

$$\frac{n^2-1}{n^2+2} = \frac{\rho_w}{\rho_w^{(0)}}\frac{n_w^2-1}{n_w^2+2} + \frac{\rho_{CO_2}}{\rho_{CO_2}^{(0)}}\frac{n_{CO_2}^2-1}{n_{CO_2}^2+2}, \tag{2.9}$$

Where $\rho_w^{(0)}$, is the density of pure water at the reference temperature and $\rho_{CO_2}^{(0)}/M_{CO_2}$ is the inverse partial molar volume of CO_2 at the relevant pressure and temperatures. We use ρ_w and ρ_{CO_2} to denote the concentrations of water and carbon dioxide. The data for the pure water and CO_2 can be found in [3], page 72, to be $\rho_{CO_2}^{(0)} = 1/\mathrm{Vco}_2 = 30.3$ mol / liter, whereas $\rho_w^{(0)} = 1/\mathrm{V_{H2O}} = 55.1$ mol / liter at 39 °C.

For ideal solutions the densities $\rho_w^{(0)}$ and $\rho_{CO_2}^{(0)}$ are constant at a given temperature, i.e., independent of the concentrations and pressure. As the sum of the volume fractions is unity we can write the relation:

$$\frac{\rho_w}{\rho_w^{(0)}} + \frac{\rho_{CO_2}}{\rho_{CO_2}^{(0)}} = 1, \tag{2.10}$$

The Clausius-Mossotti relation reads in electrostatic units,

$$\frac{n^2-1}{n^2+2} = \frac{1}{3}\rho L\alpha, \tag{2.11}$$

where α is the polarizability [m^3/molecule], $L = 6.0225 \times 10^{23}$ is Avogadro's number [molecules/mole] and ρ [moles/m^3] is the molar concentration. The refractive index n of CO_2 at atmospheric pressure and at 273.15 *K* is n = 1.000449. The density of CO_2 at atmospheric pressure and 273.15 K is $\rho_{CO_{2g}} = 44.942$ [mol/m^3]. Therefore we find that $L\alpha = 1.998 \times 10^{-5}$. Consequently, the refractive index of "pure CO_2" can be found from $L\alpha = 1.998 \times 10^{-5}$ and the density $\rho_{CO_2}^{(0)}$ by using Eq. (2.11); from which we obtain $n_{CO_2} = 1.326$. From the literature [32] we obtain for water, the 10 w/w% and the 25 w/w% brine solutions at 39oC that nw = 1.339, n10w/w% = 1.35 and n25w/w% = 1.37 (see also the data base in PHREEQC [28]. For n-decane the refractive index is 1.405 [33]).

After differentiation of Eq. (2.9) towards z and using (2.10) we obtain:

$$\begin{aligned}\frac{\partial}{\partial z}\left(\frac{n^2-1}{n^2+2}\right) &= \frac{\partial}{\partial z}\left(1-\frac{\rho_{CO_2}}{\rho_{CO_2}^{(0)}}\right)\frac{n_w^2-1}{n_w^2+2} + \frac{\partial}{\partial z}\left(\frac{\rho_{CO_2}}{\rho_{CO_2}^{(0)}}\right)\frac{n_{CO_2}^2-1}{n_{CO_2}^2+2} \\ &= \left(\frac{n_{CO_2}^2-1}{n_{CO_2}^2+2} - \frac{n_w^2-1}{n_w^2+2}\right)\frac{1}{\rho_{CO_2}^{(0)}}\frac{\partial \rho_{CO_2}}{\partial z},\end{aligned} \tag{2.12}$$

Therefore it follows that

$$\frac{\Delta I}{I} \propto \frac{1}{n}\frac{\partial n}{\partial z} = \frac{6}{(n^2+2)^2}\left(\frac{n_{CO_2}^2-1}{n_{CO_2}^2+2} - \frac{n_w^2-1}{n_w^2+2}\right)\frac{1}{\rho_{CO_2}^{(0)}}\frac{\partial \rho_{CO_2}}{\partial z}, \tag{2.13}$$

where we used reference [27] for the derivation that $1/n\ \partial n/\partial z$ is proportional to the relative intensity variation $\Delta I/I$ in the recorded Schlieren image when the knife

edge is oriented horizontally. This equation shows that the intensity fluctuations depend on the concentration gradient ($\partial_z \rho_{CO2}$) and on the difference of $(n^2 - 1)/(n^2 + 2)$ between pure water and "pure" CO_2. It is to be noted that this difference is very small for fresh water. For the salt solutions the refractive index of fresh water n_w should be replaced by the refractive index of the salt solution. For the n-decane experiments we replace n_w by the refractive index of n-decane. In these cases the term between brackets in Eq. (2.13) is much larger than for fresh water.

2.6 Experimental Results and Interpretation

Figures 2.7, 2.8, 2.9, 2.10 and 2.11 show the experimental results. Figures 2.7, 2.8 2.9 show results at decreasing salt concentrations. Figure 2.10 shows the result for oil and Fig. 2.11 presents a result at supercritical conditions for pure water. In all experiments, the z-direction is taken as pointing vertically downward and the knife cuts the beam horizontally from below. The refractive index of the carbon dioxide

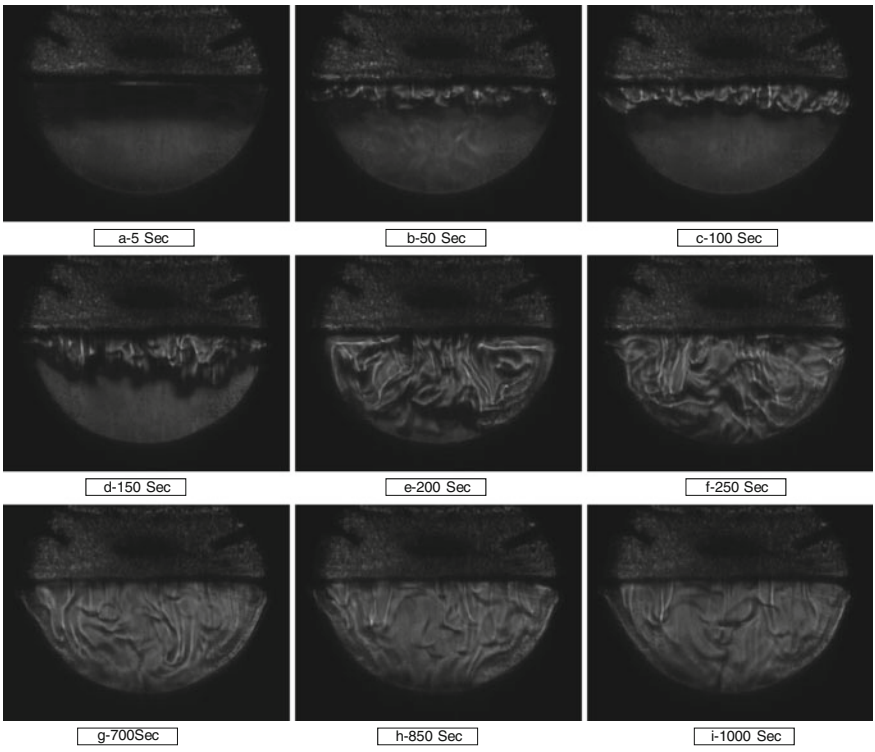


Fig. 2.7 Schlieren pattern in CO_2-Brine (25w/w% salt) after different times. It shows fingers in the lower half of the circle. The upper half is filled with CO_2 at 64 bar

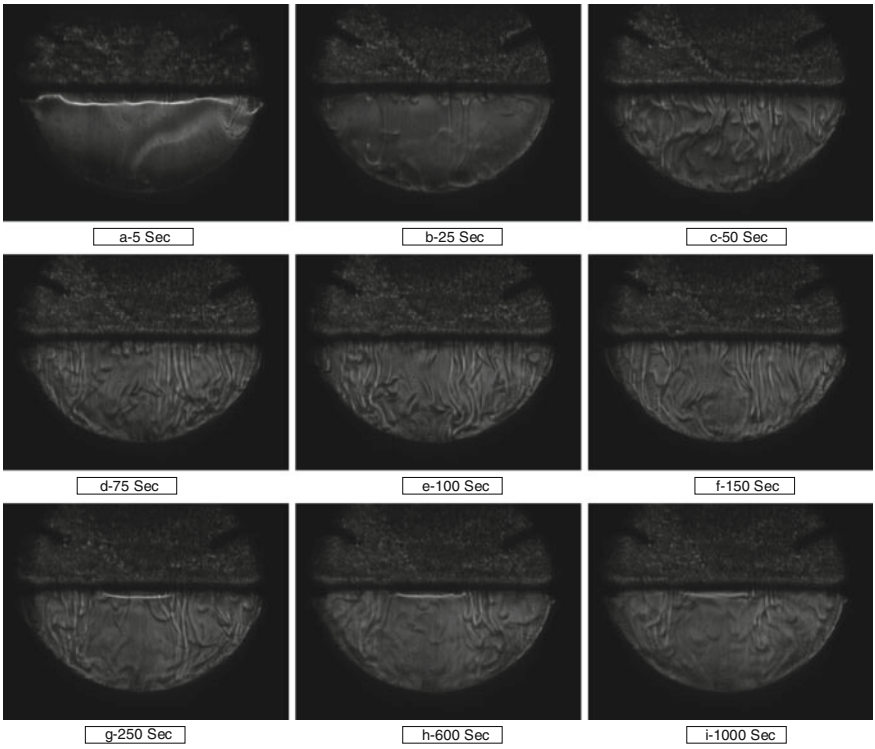


Fig. 2.8 Schlieren pattern in CO_2-Brine (10w/w% salt) after different times. It shows fingers in the lower half of the circle. The upper half is filled with CO_2 at 64 bar

containing solutions is lower than for the solutions without dissolved CO_2 (see [34]). Initially there is constant refractive index; the beam is not deflected and the observed intensity in the lower region is constant (dark grey). At later times the region below the equator appears dark as this is a region of increasing refractive index as we move downward from the equator. Indeed the beam is deflected in the direction of higher refractive index. Consequently the beam is deflected towards the knife edge and hits the knife edge. This leads to a darker region, as is observed in the experiments. At the gas-liquid interface we also expect that on average the refractive index increases from above the equator that contains a gas phase to below the equator that contains a liquid phase. This would also lead to a dark region.

Further downward, there will be fingers protruding from above in a rather erratic manner. As the light beam, which traverses in the x-direction, encounters many gravity fingers it will be deflected in all directions and shows more a typical scattering pattern and the lower half, beyond the dark region, shows an increased intensity [35–39]. So even if the beam is deflected downwards the scattered light goes around the focal point and we expect a lighter region. This is also observed in the early stages of most experiments. Still below the scattering region, diffusion of

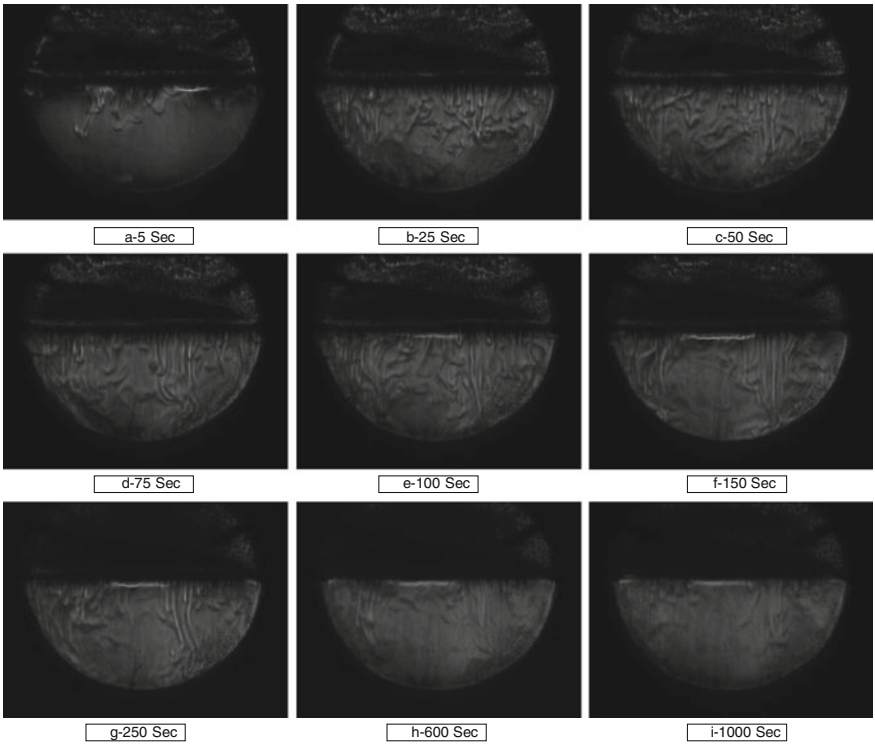


Fig. 2.9: Schlieren pattern in CO_2^- Water after different times. It shows fingers in the lower half of the circle. The upper half is filled with CO_2 at 64 bar

carbon dioxide occurs, leading again to an increasing refractive index (positive refractive index gradient) and thus to a dark region. After some time the entire region is filled with fingers. The refractive index is therefore changing erratically in the z-direction.

Figure 2.7 presents the Schlieren pattern for a 25 w/w% NaCl solution. At this high salt concentration there is only a small density contrast due to the high Henry coefficient (see Fig. 2.5) and consequently the Rayleigh number is relatively low. Moreover, according to Eq. (2.13), the refractive index contrast is larger than for pure water. The experiment starts after admitting carbon dioxide into the cell at the required pressure. Gravity fingering only initiates after 50 s. Fingers reach the bottom of the cell after about 200 s. In the early stages fingers grow much slower than in the pure water- CO_2 system (see Fig. 2.9). For $700 < t < 1000$ s the instabilities are still clearly visible in the 25 % brine case as opposed to the pure water-CO_2 system where the fingering becomes less pronounced after 1000 s.

Figure 2.8 shows the Schlieren pattern for a 10 w/w% NaCl solution. Following Eq. (2.13) we expect again that the refractive index contrast becomes larger than for pure water. One observes that fingering begins at about 25 s whereas the fingering

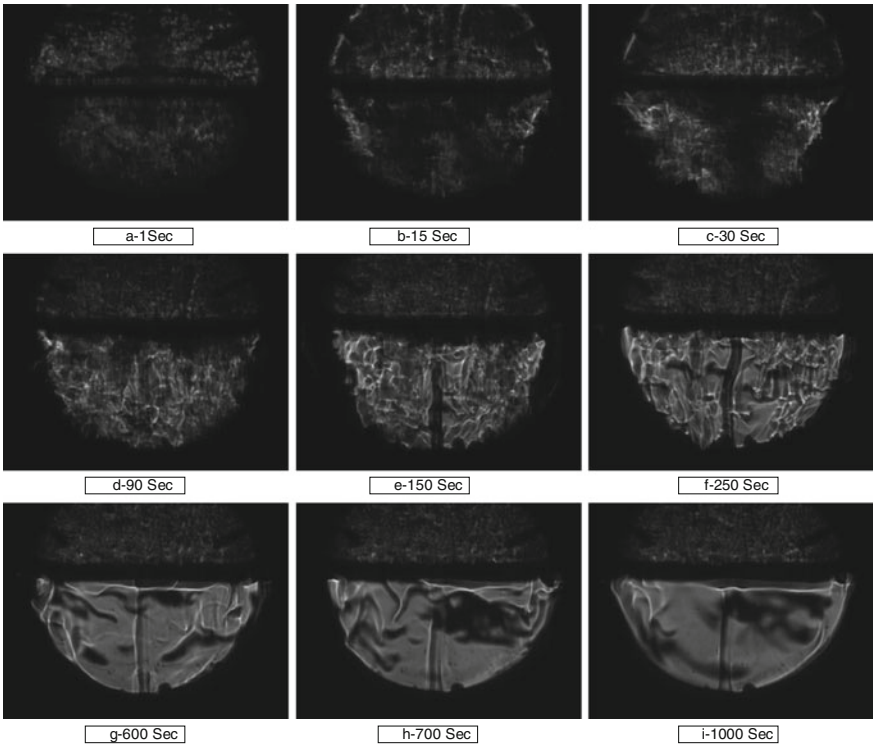


Fig. 2.10 Schlieren pattern in CO_2-Oil (nC_{10}) after different times. It shows fingers in the lower half of the circle. The upper half is filled with CO_2 at 64 bar

starts after 5 s in the CO_2 –pure water system. The time for onset of fingering is inversely proportional to Ra^{-2} [13, 16]. This means that the time for onset of gravity fingering is proportional to $(\Delta\rho)^{-2}$. The solubility of CO_2 in 10 w/w% brine is less than in pure water, but larger than in the 25 w/w% case, leading to smaller and larger $\Delta\rho$ values respectively. From t = 75 to t = 150 s a similar instability behavior is observed. As time proceeds, the speed and the number of the fingers decline. The brine- CO_2 system at later stages (600 < t < 1000 s) shows more unstable behavior than at the corresponding times in the pure water- CO_2 system.

Figure 2.9 shows the Schlieren pattern for the system of pure water- CO_2 at 64 bar. We observe that gravity fingering appears almost immediately; however, as time elapses the number of fingers and the fingering rate decreases. Figure 2.9a shows that the instabilities start from the center and then propagate towards the sides. After 25 s the instabilities are visible throughout the whole system. The fingering pattern changes constantly and stays roughly the same between t = 25 to t = 100 s. After about 100 s the fingering pattern becomes less than initially, illustrating the evolvement towards a homogeneous concentration distribution.

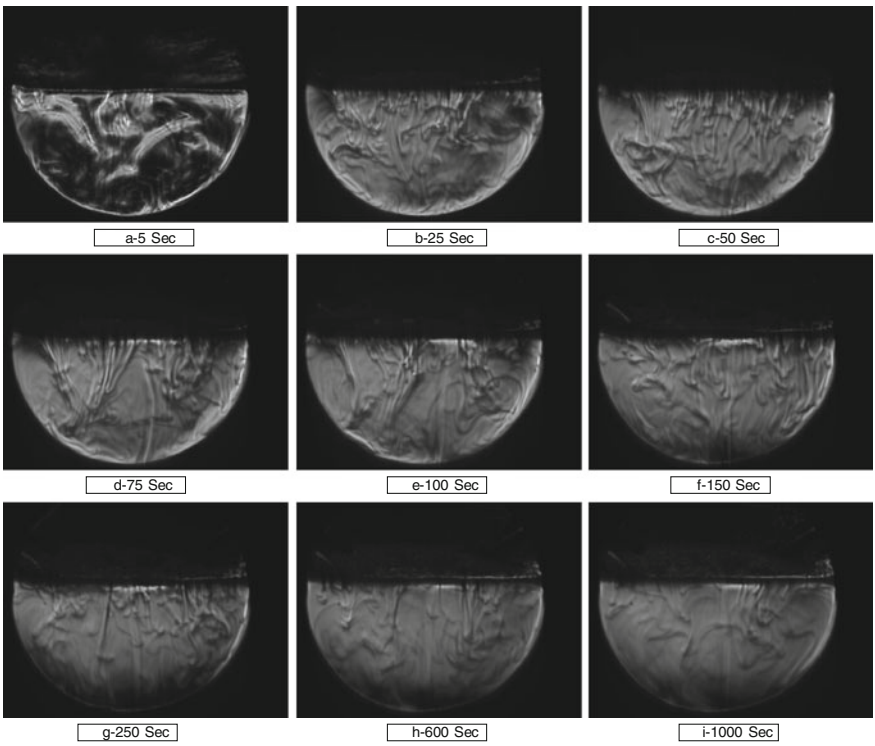


Fig. 2.11 Schlieren pattern in CO_2^- Water after different times. It shows fingers in the lower half of the circle. The upper half is filled with CO_2 at 84 bar

Figure 2.10 demonstrates the Schlieren pattern for the system of Oil (n-decane) —CO_2 at 64 bar. Immediately after bringing CO_2 on top of the oleic phase, the system exhibits highly unstable behavior. More interfacial turbulence can be seen in oil-phase experiment than in the aqueous-phase experiments. After 150 s a fingering pattern appears in the middle of the cell. From t = 600 to t = 800 s these gravity fingers are observed at both sides of the cell, albeit that the intensity of fingering becomes less. This is the first visualization experiment involving oil. We leave further interpretation of this experiment for future work.

We did an experiment at 84 bar when CO_2 in supercritical condition is brought into contact with water. Figure 2.11 shows the Schlieren pattern in the CO_2—water system after different times at 84 bar. From the beginning of injection, instability starts. After 5 s, gravity fingers hit the bottom of the cell. From t = 25 to t = 150 s the instability increases. A similar pattern persists in this period. In comparison with Fig. 2.9 at the later stages (600–1000 s), a more or less similar behavior is observed for subcritical (Fig. 2.9) and super critical CO_2 (Fig. 2.11) in contact with water.

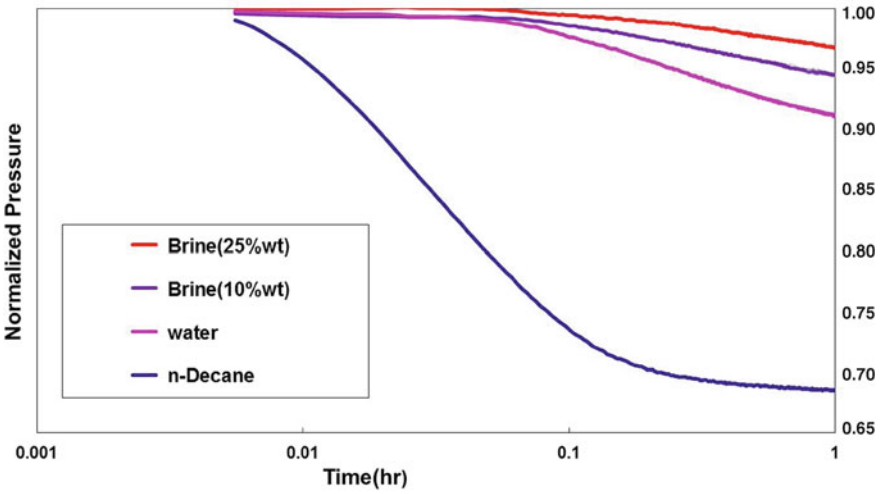


Fig. 2.12 Comparison of the pressure history of the experiments in Brine, Water and Oil at 64 bar. A pressure decrease in the upper half of the cell corresponds to a decreasing mass in the upper half of the cell, which must be for reasons of mass conservation transferred to the liquid phase in the lower half of the cell. The pressure derivative can be directly related to the integrated mass transfer rate. The "density or inverse partial molar volume" of the carbon dioxide in the liquid phase is much higher than the molar density in the gas phase, meaning that the transfer of carbon dioxide to the liquid phase entails only a negligible volume increase in the liquid phase

Figure 2.12 summarizes the pressure behavior for the four experiments at 64 bar. As shown in Fig. 2.12 the rate of pressure decline decreases in the order of oil, pure water, brine 10w/w% and finally brine 25w/w%. Indeed, due to the high miscibility of CO_2 in oil, the initial pressure decreases dramatically.

2.7 Numerical Results

The Numerical modeling of natural convection is challenging because high (spatial and temporal) resolution is required in the regions where natural convection takes place. We use commercial finite element software (COMSOL) to perform the numerical computations. For the liquid phase we apply the creeping flow equation (Eq. (2.3)), from the fluid flow module and the transport of diluted species (Eqs. (2.4), (2.5)) from the chemical species transport module. Initial and boundary conditions are given above.

Figures 2.13, 2.14, 2.15 and 2.16 show the 3-D numerical simulations corresponding to our experimental conditions. The experimental results are shown in the sequence of increasing strength of natural convection, which has as a consequence that the natural convection is the weakest for the 25w/w% salt solution, somewhat stronger at 10w/w%, again stronger for pure water (0w/w%) and strongest for the

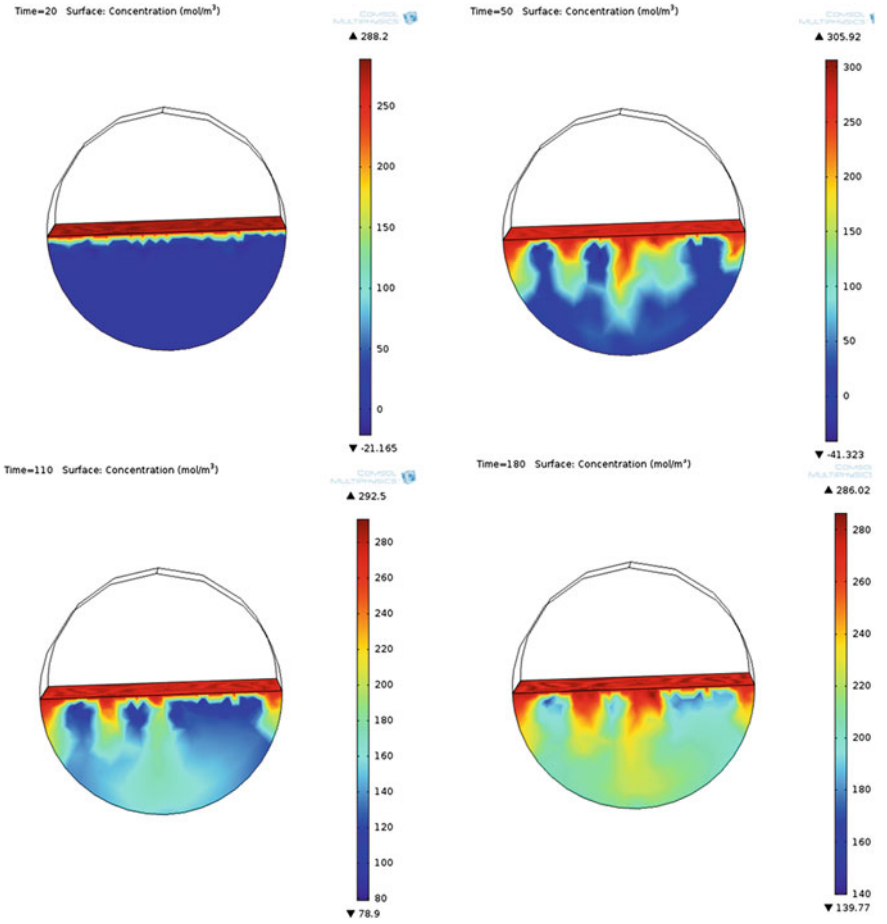


Fig. 2.13 Numerical results of classical model 25w/w% brine-CO_2 at 64 bar and 312 k,—concentration profile is shown in various times (t = 20, 50, 110 and 180 s)

n-Decane experiments. The simulations use 49876 tetrahedral elements. The elements are third order for the velocity and second order for the pressure. The elements for the concentration equation are linear.

Figure 2.13 simulates the 25 w/w% situation. The figure shows the onset of natural convection at 50 s where initial perturbation is clearly visible. The upper bound of the concentration remains more or less the same ($\sim$300 mol/m^3), but at the lower bound it increases from zero to 140 mol/m^3. As time proceeds, the fingers become longer and thicker as shown in the top right figure. Subsequently (in bottom left figure) the strength of natural convection becomes less and also the concentration contrast becomes less. The fingers persist in the right bottom figure, albeit that we note that the concentration contrast is decreasing in the range between

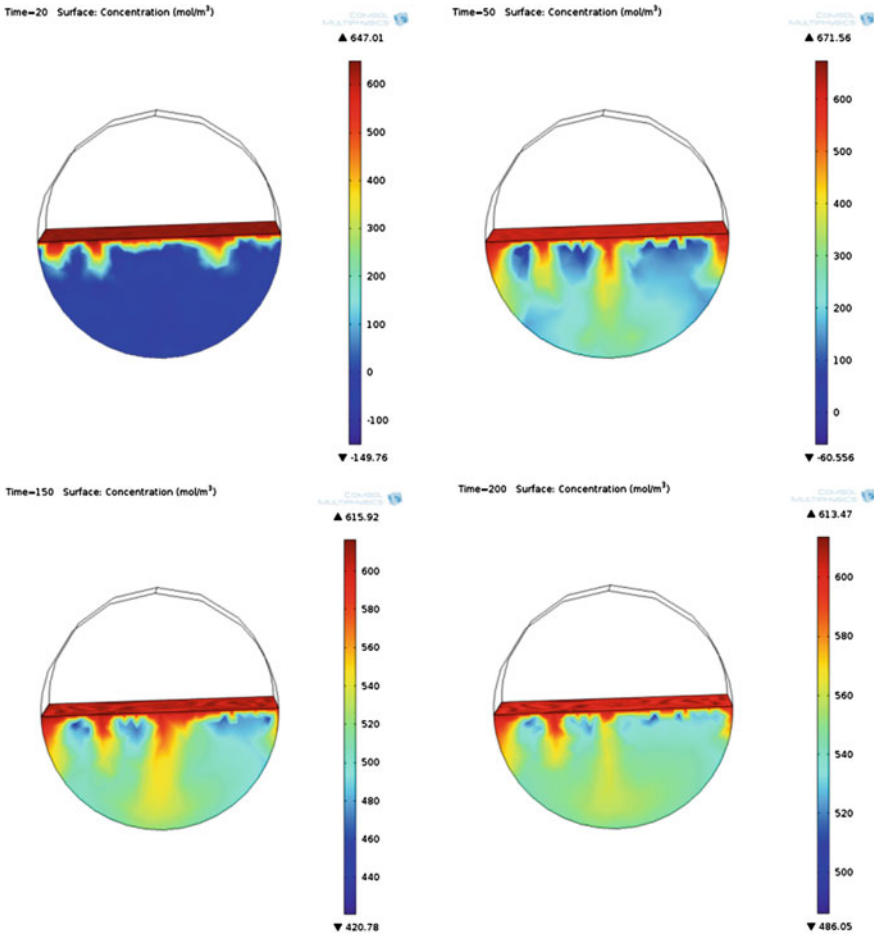


Fig. 2.14 Numerical results of classical model 10w/w%-CO_2 brine at 64 bar and 312 k,—concentration profile is shown in various times (t = 20, 50, 150 and 200 s)

140–280 mol/m^3. Figure 2.12 shows that the pressure decline for the 25 w/w% solution is slowest.

Figure 2.14 concerns the 10 w/w% situation. The top left figure shows the onset of natural convection at 20 s and the initial perturbation is already superseded by natural convection flow.

The upper bound of the concentration remains more or less the same ($\sim$700 mol/m^3), but the lower bound increases from zero to 500 mol/m^3. As time proceeds, the fingers become again longer and thicker as shown in the top right figure. Subsequently (in the bottom left figure) the strength of natural convection becomes less and also the concentration contrast becomes less. The fingers persist in the right bottom figure, albeit we note that the concentration contrast is

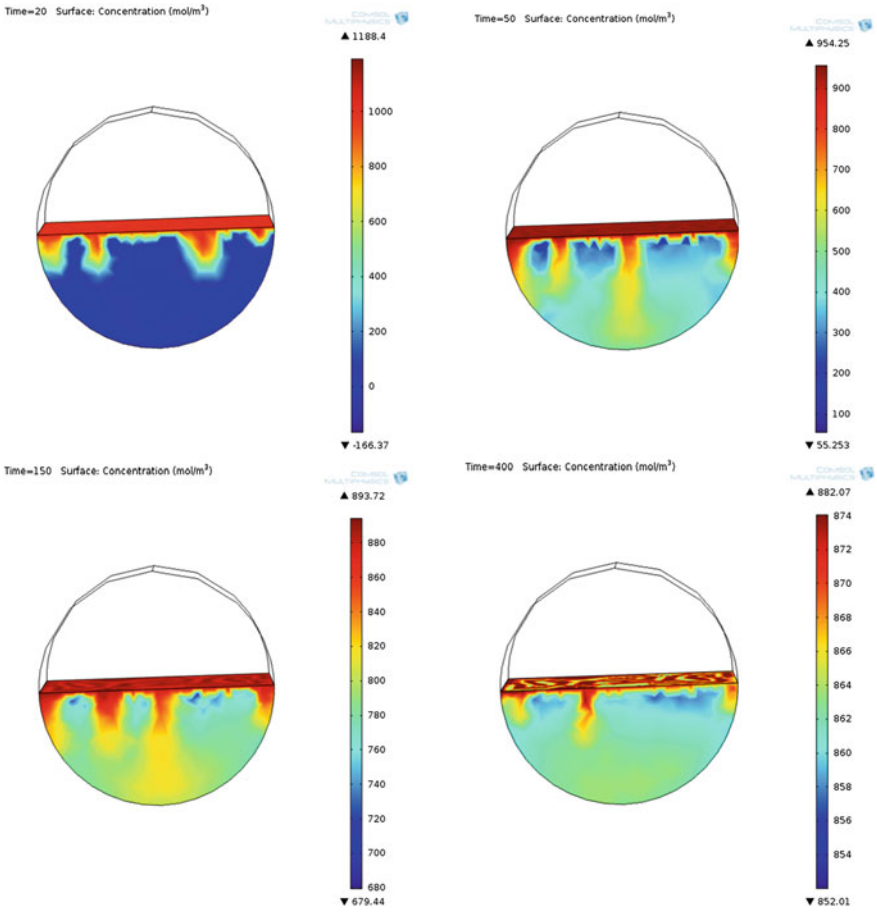


Fig. 2.15 Numerical results of classical model pure water-CO_2 at 64 bar and 312 k,—concentration profile is shown in various times (t = 20, 50, 150 and 400 s)

decreasing in the range between 500–700 mol/m^3. Figure 2.12 shows that the pressure decline for the 10 w/w% solution is the second slowest.

Figure 2.15 concerns the pure water phase. The top left figure shows the onset of natural convection at 10 s and the initial perturbation is completely superseded by natural convection flow.

The upper bound of the concentration decreases from ($\sim$1200 mol/m^3) to ($\sim$900 mol/m^3), whereas the lower bound increases from zero to ($\sim$860 mol/m^3). As time proceeds, the fingers stay more or less the same as shown in the top right figure. Subsequently (in bottom left figure) the strength of natural convection becomes less and also the concentration contrast becomes less. The fingers almost disappear in the right bottom figure, which is even more conspicuous if we consider that the concentration contrast is decreasing in the range between

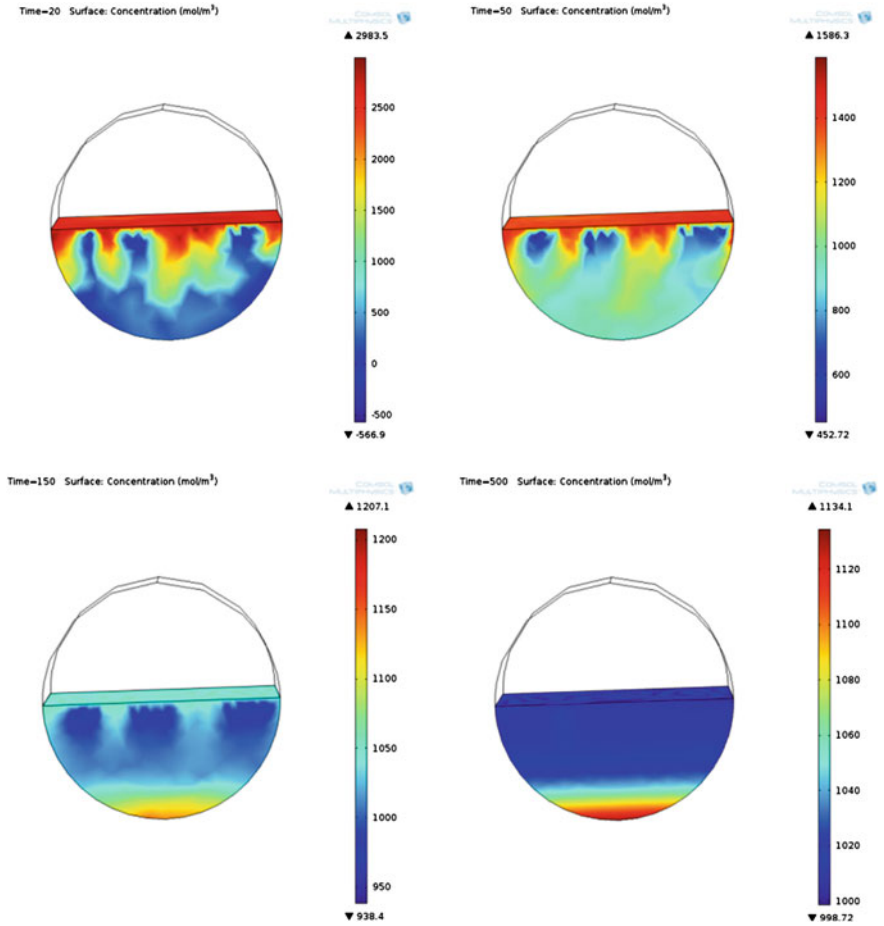


Fig. 2.16 Numerical results of classical model Decane-CO_2 at 64 bar and 312 K,—concentration profile is shown in various times (t = 20, 50, 150 and 500 s)

(854–874 mol/m^3). Figure 2.12 shows that the pressure decline for the 0 w/w% solution is stronger than for the 10 w/w% solution.

Figure 2.16 shows the numerical simulation for the oleic phase. The top left figure shows that the on-set of natural convection occurs at 20 s.

The upper bound of the concentration decreases from ($\sim$2700 mol/m^3) to (1400 mol/m^3), whereas the lower bound increases from zero to (1000 mol/m^3). As time increases the fingers become less conspicuous. Figure 2.12 shows that the pressure decline for oleic phase is stronger than for the other cases.

Figure 2.17 compares the measured pressure history with results obtained with numerical simulation. The computed results show qualitatively the same trends as the experimental results albeit that the computed transfer rate is larger.

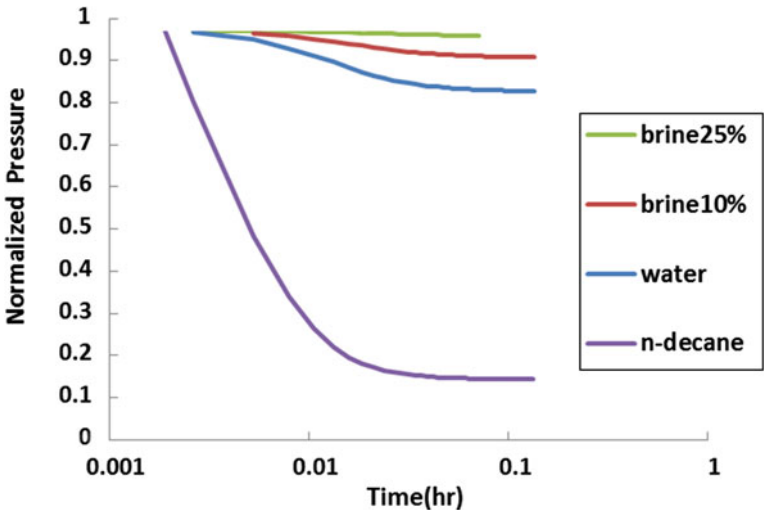


Fig. 2.17 Comparison of the pressure history of the modeling in Brine, Water and Oil at 64 bar

This is in particular conspicuous for the oil result. Indeed, comparison of the experimental results to the numerical results shows only qualitative agreement. We conjecture in the numerical section that the grid cells are too large to capture the mm-scale fine structure of the gravity fingers. It is technically not possible to use smaller grid cells as this will lead to prohibitively long computation times. In comparison to the onset of instability there is some correspondence between experiments and numerical results. In the numerical model, the number of fingers is much less than in the experimental results. Also in the numerical calculations the fingers are much larger. The main qualitative correspondence between simulations and experiments is that there is a region of high concentration gradient near the gas–liquid interface. We leave simulations with finer grids for a better understanding to future work.

2.8 Conclusions

- Dissolution of CO_2 in an aqueous (or oleic) phase forms a mixture that is denser than the carbon dioxide free water or brine (oleic phase). This causes a local density increase, which induces natural convection currents (gravity fingers) when gaseous carbon dioxide is brought above the liquid phase. This enhances the rate of mixing of CO_2 in the liquid phase.
- We designed and built a cylindrical transparent high pressure cell in which gravity induced fingers (playing a major role in the enhanced mixing process) could be observed, e.g., by mounting the cylinder horizontally and filling the

bottom half with liquid and the top-half with gaseous or supercritical carbon dioxide.

- We developed a Schlieren set-up that can be used to observe the gravity induced fingers based on refractive index variations. Gravity fingers have been observed in an aqueous phase with various concentrations of sodium chloride (0–25 w/w %) or with an oleic phase (n-decane). The experiments show that natural convection currents are weakest in highly concentrated brine and strongest in oil.
- The Schlieren pattern consists of a dark region near the equator and a lighter region below it. The dark region indicates a region where the refractive index increases downward, either due to the presence of a gas liquid interface, or due to the thin diffusion layer, which also appears in numerical simulations.
- It is possible to use commercial software (COMSOL Multiphysics) to simulate the natural convection process in 3-D albeit with grid cells that are too large to capture the mm-scale fine structure of the gravity fingers. As the distance between the windows is 11.6 mm it can be expected that the concentration is not uniform in the axial direction. This leads initially to a scattering region with a lighter appearance in the Schlieren pattern. For later times the erratic behavior decreases and the effect of individual gravity fingers can be observed.
- To our knowledge this is the first time that gravity fingers in the oil phase are visualized. The set-up can screen any fluid for its relative importance of natural convection flows.

References

1. Eftekhari, A. A., Van Der Kooi, H., & Bruining, H. (2012). Exergy analysis of underground coal gasification with simultaneous storage of carbon dioxide. *Energy, 45*(1), 729–745.
2. Van der Meer, L. (1992). Investigations regarding the storage of carbon dioxide in aquifers in the Netherlands. *Energy Conversion and Management, 33*(5), 611–618.
3. Gmelin, L. (1973). *Gmelin Handbuch der anorganischen Chemie, 8. Auflage. Kohlenstoff, Teil C3, Verbindungen.* ISBN 3-527-81419-1.
4. Bachu, S., Gunter, W., & Perkins, E. (1994). Aquifer disposal of CO_2: Hydrodynamic and mineral trapping. *Energy Conversion and Management, 35*(4), 269–279.
5. Class, H., et al. (2009). A benchmark study on problems related to CO_2 storage in geologic formations. *Computational Geosciences, 13*(4), 409–434.
6. Elder, J. (1968). The unstable thermal interface. *Journal of Fluid Mechanics, 32*(1), 69–96.
7. Ennis-King, J., Preston, I., & Paterson, L. (2005). Onset of convection in anisotropic porous media subject to a rapid change in boundary conditions. *Physics of Fluids 17*(8), 084107–084107-15.
8. Foster, T. D. (1965). Onset of convection in a layer of fluid cooled from above. *Physics of Fluids, 8*, 1770.
9. Gasda, S. E. (2010). Numerical models for evaluating CO_2 storage in deep saline aquifers: Leaky wells and large-scale geological features. *Ph.D. Thesis*. http://arks.princeton.edu/ark:/88435/dsp01j098zb09n.
10. Nordbotten, J. M., & Celia, M. A. (2011). *Geological Storage of CO_2: Modeling Approaches for Large-Scale Simulation*2011: Wiley. com.

11. Nordbotten, J. M., Celia, M. A., & Bachu, S. (2005). Injection and storage of CO_2 in deep saline aquifers: Analytical solution for CO_2 plume evolution during injection. *Transport in Porous Media, 58*(3), 339–360.
12. Ranganathan, P., et al. (2012). Numerical simulation of natural convection in heterogeneous porous media for CO_2 geological storage. *Transport in Porous Media, 95*(1), 25–54.
13. Riaz, A., et al. (2006). Onset of convection in a gravitationally unstable diffusive boundary layer in porous media. *Journal of Fluid Mechanics, 548*, 87–111.
14. Walker, K. L., & Homsy, G.M. (1978). Convection in a porous cavity. Journal of Fluid Mechanics, *87*(Part 3), 449–474.
15. Van Duijn, C., Pieters, G., & Raats, P. (2004). Steady flows in unsaturated soils are stable. *Transport in Porous Media, 57*(2), 215–244.
16. Meulenbroek, B., Farajzadeh, R., & Bruining, H. (2013). The effect of interface movement and viscosity variation on the stability of a diffusive interface between aqueous and gaseous CO_2. *Physics of Fluids (1994-present) 25*(7), 074103.
17. Myint, P. C., & Firoozabadi, A. (2013). Onset of convection with fluid compressibility and interface movement. *Physics of Fluids, 25*, 094105.
18. Lapwood, E. (1948). Convection of a fluid in a porous medium. *Proceedings of the Cambridge*.
19. Weir, G., White, S., & Kissling, W. (1995). Reservoir storage and containment of greenhouse gases. *Energy Conversion and Management, 36*(6), 531–534.
20. Farajzadeh, R., et al. (2007). Mass transfer of CO_2 into water and surfactant solutions. *Petroleum Science and Technology, 25*(12), 1493–1511.
21. Farajzadeh, R., et al. (2007). Numerical simulation of density-driven natural convection in porous media with application for CO_2 injection projects. *International Journal of Heat and Mass Transfer, 50*(25), 5054–5064.
22. Farajzadeh, R., Zitha, P. L., & Bruining, J. (2009). Enhanced mass transfer of CO_2 into water: Experiment and modeling. *Industrial and Engineering Chemistry Research, 48*(13), 6423–6431.
23. Yang, C., & Gu, Y. (2006). Accelerated mass transfer of CO_2 in reservoir brine due to density-driven natural convection at high pressures and elevated temperatures. *Industrial and Engineering Chemistry Research, 45*(8), 2430–2436.
24. Nazari Moghaddam, R., & Rostami, B. (2012). Reply to the "Comments on the paper 'Quantification of density-driven natural convection for dissolution mechanism in CO_2 sequestration' by R. Nazari Moghaddam et al. (2011)". Transport in Porous Media, *93*(1), 175–178.
25. Okhotsimskii, A., & Hozawa, M. (1998). Schlieren visualization of natural convection in binary gas–liquid systems. *Chemical Engineering Science, 53*(14), 2547–2573.
26. Kneafsey, T. J., & Pruess, K. (2010). Laboratory flow experiments for visualizing carbon dioxide-induced, density-driven brine convection. *Transport in Porous Media, 82*(1), 123–139.
27. Settles, G. S. (2001). *Schlieren and Shadowgraph Techniques: Visualizing Phenomena in Transparent Media. 2001.* Berlin: Springer.
28. Parkhurst, D. L., & Appelo, C. (2013). *Description of input and examples for PHREEQC version 3- A computer program for speciation, batch-reaction, one-dimensional transport, and inverse geochemical calculations.* US Geological Survey Techniques and Methods, Book 6, Modeling Techniques, 2013.
29. Randall, M., & Failey, C. F. (1927). The Activity Coefficient of Gases in Aqueous Salt Solutions. *Chemical Reviews, 4*(3), 271–284.
30. Feynman, R., Leighten, R., & Sands, M. (1965). *The Feynman Lectures on Physics.* Reading: Addison-Wesley Pub. Comp.
31. Song, Y., et al. (2003). Measurement on CO_2 Solution Density by Optical Technology. *Journal of Visualization, 6*(1), 41–51.

32. Subedi, D., et al. (2006). Study of temperature and concentration dependence of refractive index of liquids using a novel technique. *Kathmandu University Journal of Science, Engineering and Technology, 2*(1), 1–7.
33. Mosteiro, L., et al. (2001). Density, speed of sound, refractive index and dielectric permittivity of (diethyl carbonate+ n-decane) at several temperatures. *The Journal of Chemical Thermodynamics, 33*(7), 787–801.
34. Bao, B., et al. (2012). Detecting Supercritical CO_2 in Brine at Sequestration Pressure with an Optical Fiber Sensor. *Environmental Science and Technology, 47*(1), 306–313.
35. Gatej, A., Wasselowski, J., & Loosen, P. (2012). Using adaptive weighted least squares approximation for coupling thermal and optical simulation. *Applied Optics, 51*(28), 6718–6725.
36. Rimmer, M.P. (1983). *Ray tracing in inhomogeneous media*. in *1983 International Technical Conference/Europe*. International Society for Optics and Photonics.
37. Sharma, A., Kumar, D. V., & Ghatak, A. K. (1982). Tracing rays through graded-index media: A new method. *Applied Optics, 21*(6), 984–987.
38. van der Net, A., et al. (2007). Simulating and interpretating images of foams with computational ray-tracing techniques. *Colloids and Surfaces A: Physicochemical and Engineering Aspects, 309*(1), 159–176.
39. Wu, Z. S., et al. (1997). Improved algorithm for electromagnetic scattering of plane waves and shaped beams by multilayered spheres. *Applied Optics, 36*(21), 5188–5198.

http://www.springer.com/978-3-319-23086-3

Mechanisms for CO2 Sequestration in Geological Formations and Enhanced Gas Recovery

Khosrokhavar, R.

2016, XVI, 94 p. 39 illus., 26 illus. in color., Hardcover
ISBN: 978-3-319-23086-3